The Meteoritical Society

Meteoritics & Planetary Science 43, Nr 6, 997–1007 (2008)
Abstract available online at http://meteoritics.org

Numerical simulation of a permittivity probe for measuring the electric properties of planetary regolith and application to the near-surface region of asteroids and comets

Klaus SPITZER[1], Frank SOHL[2], and Martin PANZNER[1, 3]

[1]Institute of Geophysics, Technische Universität Bergakademie Freiberg, Gustav-Zeuner-Str. 12, Freiberg 09596, Germany
[2]Institute of Planetary Research, German Aerospace Center (DLR), Berlin-Adlershof, Germany
[3]Present address: EMGS AS, Trondheim, Norway
[*]Corresponding author. E-mail: klaus.spitzer@geophysik.tu-freiberg.de

(Received 13 March 2007; revision accepted 19 December 2007)

Abstract–We present a numerical simulation technique for the retrieval of the electric properties relative permittivity and conductivity of planetary, asteroid, and cometary regolith. Our simulation techniques aim at accompanying hardware development and conducting virtual experiments, e.g., to assess the response of arbitrary heterogeneous conductivity and permittivity distributions or to scrutinize possibilities for spatial reconstruction methods using inverse schemes. In a first step, we have developed a finite element simulation code on the basis of unstructured, adaptive triangular grids for arbitrary two-dimensional axisymmetric distributions of conductivity and permittivity. The code is able to take into account the spatial geometry of the probe and allows for possible inductive effects. In previous studies, the non-inductive approach has been used to convert potential and phase data into apparent material properties. By our simulations, we have shown that this approach is valid for the frequency range from 10^2 Hz to 10^7 Hz and electric conductivities of 10^{-8} S/m that are typical for the near-surface region of asteroids and comets composed of chondritic materials and/or frozen volatiles such as H_2O and CO_2 ice. We prove the accuracy of our code to be better than 10%, using mixed types of boundary conditions and present a simulated vertical log through a horizontally stratified subsurface layer as a representative example of a heterogeneous distribution of the electrical properties. Resolution studies for the given electrode separation reveal that the material parameters of layers having thicknesses of less than about half the electrode spread are not reconstructible if only apparent quantities are considered. Therefore, spatial distributions of the complex sensitivity are presented having in mind a future data inversion concept that will permit the multi-dimensional reconstruction of material parameters in heterogeneous environments.

INTRODUCTION

Near-Earth asteroids and cometary nuclei provide important clues to the early formation and initial composition of larger solar system bodies. The surface and subsurface of asteroids and cometary nuclei have experienced numerous cycles of regolith development. While asteroid surfaces are heavily cratered and fragmented by meteoritic impacts, and subsequently modified by space weathering processes (Chapman 2004), cometary nuclei are believed to be modified by cosmic particle bombardment and erosion due to the more intense solar insolation they experience in the inner solar system. Spacecraft observations acquired during recent asteroid encounters support the notion of Housen and Wilkening (1982) that larger bodies are often covered by substantial regolith layers, whereas small rocky asteroids may develop only negligible near-surface layers (e.g., Veverka et al. 2001; Yano et al. 2006). Asteroid regolith is expected to be stratified as a consequence of impact fragmentation and deposition of discrete layers of widely spread ejecta. In turn, the formation of cometary regolith is likely linked to dust particles that are locally released in the process of sublimation of volatiles and deposited in remote inactive regions (Möhlmann 1994). However, sublimated ices will not only evaporate from the primordial surface, but they tend to flow inward, thereby causing compositional fractionation and layering of the cometary subsurface (Benkhoff and Huebner 1995).

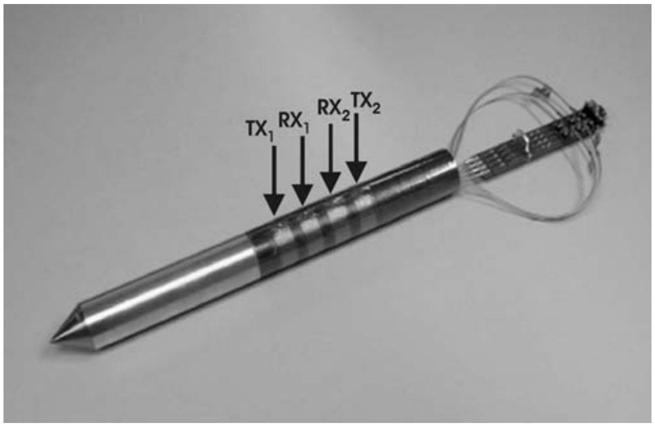

Fig. 1. Prototype of the permittivity probe according to Trautner and Grard (2002). TX and RX represent two pairs of transmitter and receiver electrodes, each consisting of a metallic winding wrapped around an insulating cylinder.

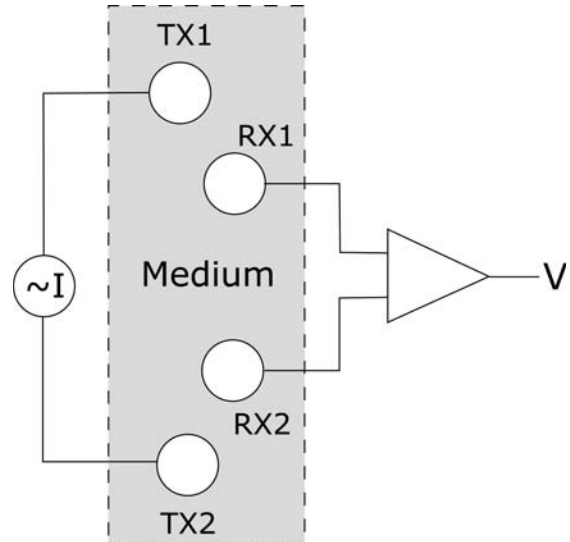

Fig. 2. Block diagram of the four-electrode permittivity probe. The transmitter electrodes TX1 and TX2 are connected to an alternating current source *I* of constant amplitude. The receiver electrodes RX1 and RX2 measure the induced voltage *V*. The transfer impedance of the quadrupolar array is obtained from the ratio between *V* and *I*.

The Comet Nucleus Sounding Experiment by Radiowave Transmission (CONSERT) on board the Rosetta mission is intended to probe the nucleus of the mission's target comet 67P/Churyumov-Gerasimenko, monitoring the propagation of long-wavelength radar signals transmitted from the orbiter and returned from the Philae lander, to determine the interior structure, chemical composition, and physical properties of a cometary nucleus (Kofman et al. 1998, 2007). Philae will be placed on the cometary surface in 2014, carrying among other instruments the Surface Electric Sounding and Acoustic Monitoring Experiment (SESAME), a subsurface science experiment package aimed at measuring the mechanical and electrical properties of the cometary near-surface layer as well as those of particles released from the surface (Seidensticker et al. 2007). Together with energy balance information, derived in parallel from thermal measurements of the multi-purpose sensor package MUPUS, new important constraints are expected on the modification of cometary surface material and internal heat transfer as the comet approaches perihelion (Spohn et al. 2007).

A well-suited device for in-situ measurements of the physical properties and the stratification of planetary, asteroid, and cometary regolith is a self-inserting cone penetrometer or mole equipped with an internal hammering mechanism that permits to intrude into moderately compact soil to displace embedded rocks and pebbles, and to even fracture sintered ice grains (Kochan et al. 2001). For example, the electromechanical PLUTO mole on board the ill-fated Beagle 2 mission was intended to establish a Martian subsurface stratigraphy near the landing site by collecting multiple soil samples and retrieval for later analysis (Richter et al. 2002). Currently, lightweight self-inserting instrumented mole systems for the deployment of specifically tailored sensor packages to depths of several meters are under development to compass in-situ measurements of physical key properties of layered regoliths. These include deduced dielectric properties like relative permittivity and electric conductivity, thermophysical properties, and inferred and/or measured cohesion of near-surface materials.

In the following, a numerical simulation technique is presented that goes along with the development of a probe for measuring the electric properties conductivity and permittivity of planetary, asteroid, and cometary regoliths.

METHODOLOGY

A mole-carried prototype of a low-power probe (Fig. 1) has been developed by Trautner and Grard (2002) for measuring electric conductivity and permittivity as a complex quantity in the frequency domain. So far, the existing prototype, whose development was supported by the European Space Agency, has exclusively been tested in the laboratory using polyethylene, quartz glass beads or a Mars soil simulant called JSC-1. The laboratory tests indicate that the average measurement precision is about 20% with respect to calibrated reference measurements owing to current measurement circuitry, limited phase measurement accuracy, accuracy of representative circuit models, and parasitic capacitances (Trautner et al. 2004). The probe is designed to record a vertical profile while being hammered into the ground by a self-inserting mechanism. The electric coupling is rendered capacitively via two pairs of ring electrodes for the transmitter TX and the receiver RX (Fig. 2).

Measurement Principle

Early works on capacitively coupled devices go back to Grard (1990). In contrast to self-impedance measurements, mutual impedance measurements have the advantage of being less sensitive to imperfect coupling between the electrodes and the ground (Hamelin et al. 2004). The injected alternating current of approximately $I_0 = 10^{-9}$ A at frequencies in the kHz range is mainly dielectric since the electric conductivity of geologic materials is generally low in the absence of electrochemical reactions. The electrical conductivity of terrestrial rocks and sediments in the presence of moisture is about 10 mS/m (Grard 1990) and range from 10^{-9} to 10^{-10} S/m for dry lunar-type regolith at a frequency of 1 kHz (Carrier et al. 1991). Thus, dielectric losses are negligible, even at the highest frequency, and the dielectric constant certainly dominates permittivity measurements in dry, porous regolith (Martinez and Byrnes 2001; Pettinelli et al. 2003).

The extremely low conductivity of regolith yields a voltage signal on the order of mV, which is recorded by the ring electrodes RX. The transmitter and receiver electrodes TX and RX are lined up in a classical equidistant 4-point arrangement along the cylindrical body of the probe (Fig. 1). Power consumption totals only 80 mW. The potential measurements are interpreted in a non-inductive mode. Using a reference measurement for vacuum, the apparent relative permittivity ε_r^a and the apparent electric conductivity σ^a are determined by

$$\varepsilon_r^a = \frac{|\Delta V_0|}{|\Delta V|} . \cos(\phi_0 - \phi) \tag{1}$$

$$\sigma^a = -\frac{|\Delta V_0|}{|\Delta V|} . \omega\varepsilon_0 . \sin(\phi_0 - \phi) \tag{2}$$

where ΔV_0 and ϕ_0 are the reference potential difference and phase for vacuum and ΔV and ϕ are the corresponding quantities in an arbitrary medium. ε_0 is the dielectric constant and ω is the angular frequency, chosen such that the resultant wavelength is much larger than the size of the electrode array. Strictly speaking, Equations 1 and 2 are only valid for a plate capacitor or on the connecting line between two poles if no induction currents are generated. In case of homogeneous materials, these equations then reflect the true material parameters.

Numerical Modeling Approach

In order to comprehensively describe the nature of the physical problem we have to take into account the coupling of the electric and magnetic fields $\vec{E}$ and $\vec{H}$. We therefore introduce the magnetic vector potential $\vec{A}$ giving

$$\vec{E} = -\nabla V - \frac{\partial \vec{A}}{\partial t} \tag{3}$$

$$\vec{H} = \frac{1}{\mu_0 \mu_r} \nabla \times \vec{A}, \tag{4}$$

where μ_0 is the free space magnetic permeability, μ_r the relative magnetic permeability, t the time, and V the electric potential. To completely describe the behavior of low-frequency electromagnetic fields in a source-free, conductive, and polarizable medium, we have to solve the equation of continuity augmented by the dielectric displacement current and Ampere's law. In the frequency domain they read

$$\nabla \cdot \vec{j} = 0 = \nabla \cdot [(\sigma + i\omega\varepsilon_0\varepsilon_r)\nabla V] \tag{5}$$

$$\nabla \times \vec{H} = \vec{j} = (\sigma + i\omega\varepsilon_0\varepsilon_r)\nabla V, \tag{6}$$

where $\vec{j}$ is the electric current density, ε_r the relative electric permittivity, σ the electric conductivity, and i the imaginary unit. Substituting Equations 3 and 4 into Equations 5 and 6, setting the complex valued conductivity $\tilde{\sigma} = (\sigma + i\omega\varepsilon_0\varepsilon_r)$ and the magnetic permeability $\mu = \mu_0\mu_r$, we obtain the governing coupled system of equations

$$-\nabla \cdot [i\omega\tilde{\sigma}\vec{A} + \tilde{\sigma}\nabla V] = 0 \tag{7}$$

$$i\omega\tilde{\sigma}\vec{A} + \nabla \times \left(\frac{1}{\mu}\nabla \times \vec{A}\right) + \tilde{\sigma}\nabla V = 0, \tag{8}$$

the finite element discretization of which is provided in Appendix A.

Accuracy and Adaptive Grid

In the contact area of the electrodes, large conductivity contrasts exist (copper/regolith) which produce notable gradients of the electric potential. Therefore, in this region the unstructured triangular grid has adaptively been refined to a high degree (Fig. 3). This is of particular concern, because the measurement of the potential difference is carried out at the potential electrodes RX. We have checked the accuracy of our code by comparison with the analytic solution for a vertical electric dipole in a homogeneous medium and the frequency of 1 kHz (Telford et al. 1995). The model domain is a cylinder of $r = 2$ m radius and $H = 2$ m height. Figure 4 shows the orientation of the dipole and field properties (a) and the results for Dirichlet and mixed boundary conditions (b) in comparison with the analytic solution. Note the good agreement (<10%) for the latter within the whole domain except for the region close to the singularity ($r < 0.2$ m). The accuracy may be increased by using finer discretizations at the cost of larger memory requirements.

Figure 5 presents numerical simulations of the potential ΔV and phase ϕ measured at the receiver electrodes *RX* within the frequency range of 1 Hz to 10^{10} Hz (two upper subplots). Using Equations 1 and 2, the apparent quantities permittivity ε_r^a and conductivity σ^a are determined (two lower subplots). For simplicity, the model is homogeneous with a conductivity $\sigma = 10^{-8}$ S/m and permittivity $\varepsilon_r = 4$. The latter is consistent with measured dielectric properties of meteoritic samples and dust-enriched porous mixtures of ice and meteoritic dust that

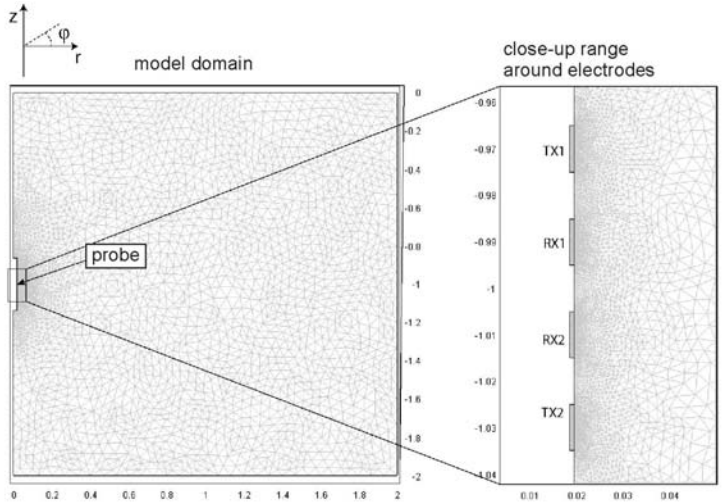

Fig. 3. Discretization of the model domain. Two-dimensional cylindrical symmetry about the axis of an electrically isolating probe is assumed. The grid is strongly refined close to the transmitter and receiver electrodes.

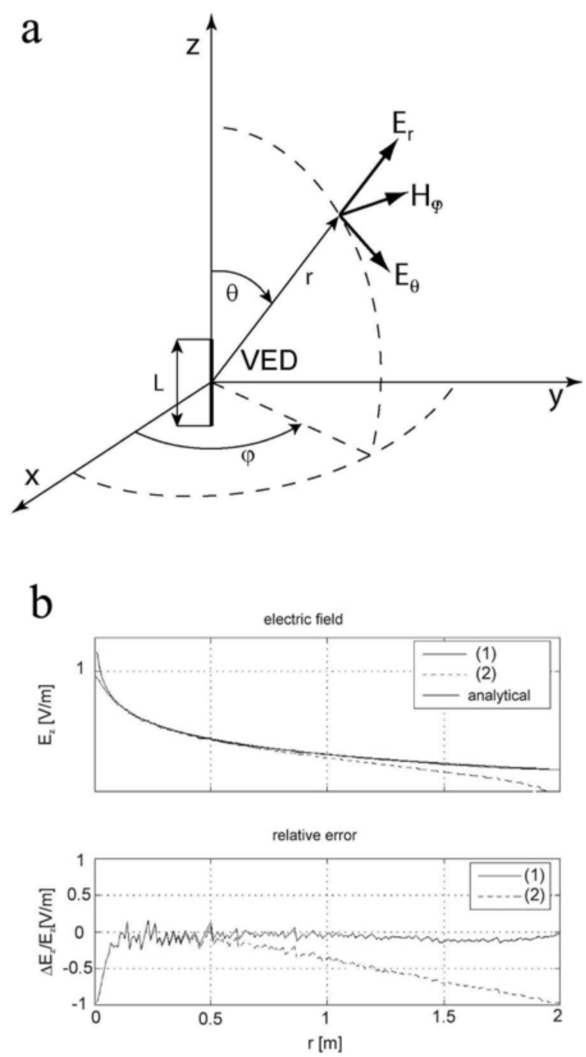

Fig. 4. a) Schematic representation of a vertical electric dipole (VED) and corresponding field properties. b) *z* component of the electric field $\overrightarrow{E_z}$ and its relative error $\Delta\overrightarrow{E_z}/\overrightarrow{E_z}$ in the equatorial plane as a function of the distance *r* to the dipole center for 1) mixed boundary conditions and 2) Dirichlet boundary conditions.

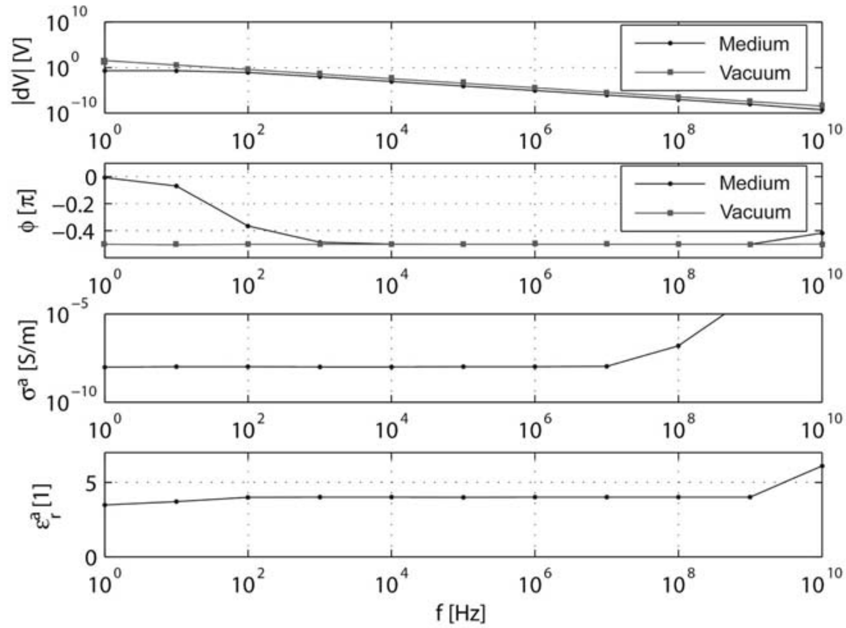

Fig. 5. From top to bottom: numerically calculated potential difference at the receiver electrodes $|\Delta V|$, phase ϕ, apparent conductivity σ^a, and apparent permittivity ε_r^a. The frequency range reaches from 1 Hz to 10^{10} Hz. The apparent quantities reflect those prescribed in the frequency range $10^2 < f < 10^7$ for the given conductivity $\sigma = 10^{-8}$ S/m and permittivity $\varepsilon_r = 4$. The deviations at the low and high frequency ends are only due to numerical instabilities.

serve as compositional analogs of asteroid- and comet-nucleus-like surface materials (Heggy et al. 2006; Carley and Heggy 2007). In the frequency range 10^2 Hz $< f < 10^7$ Hz the model response is stable and apparent conductivity and permittivity agree with the material parameters. At the low ($f < 10^2$ Hz) and high frequency end ($f > 10^7$ Hz), the problem becomes numerically instable. For high frequencies $f > 10^7$ Hz the applied current is nearly completely dielectric, i.e., the imaginary part of the complex conductivity Im $(\tilde{\sigma}) = i\omega\varepsilon_0\varepsilon_r$ dominates the real part Re $(\tilde{\sigma}) = \sigma$ by several orders of magnitude. For low frequencies $f < 10^2$ Hz the conduction current thus becomes more important. Then, the substantial conductivity contrast between copper-electrode ($\sigma_{\mathrm{Cu}} = 5.9 \times 10^7$ S/m) and surrounding medium ($\sigma_{\mathrm{Regolith}} \approx 10^{-8}$ S/m) leads to a large condition number of the system matrix, which again tends to numerical instabilities.

The frequency range 10^2 Hz $< f < 10^6$ Hz is characterized by low induction numbers $B << 1$ (Benderitter et al. 1994), where inductive effects are negligible. The induction number is defined by $B = L/p$ with a typical scale length L of the measurement and the electromagnetic skin depth p. For the investigated medium with conductivity ($\sigma_{\mathrm{Regolith}} \approx 10^{-8}$ S/m), the skin depth $p \approx 500$ km for $f = 10^2$ Hz and $p \approx 1.6$ km for $f = 10^7$ Hz. The scale length of the electrode array is $L = 7$ cm giving induction numbers $B \approx 10^{-7}$ and $B \approx 10^{-5}$ for the low and high frequency, respectively.

The first string of our numerical developments and investigations aim at inspecting the validity of this formulation in conjunction with the permittivity probe taking into account its deviations from perfect conditions, i.e., its explicit cylindrical geometry and the perturbation it applies to the probed medium while penetrating. The second string aims at resolution studies in terms of sensitivities and detectability of regolith stratification.

NUMERICAL SIMULATION

In the following, we consider a simple but meaningful model of a horizontally stratified cometary subsurface of anomalous electric properties being penetrated by the probe in the vertical direction (Fig. 6a). While moving downwards, the probe records a vertical profile of the apparent complex conductivity comparable to a terrestrial borehole log. For simplicity, the probe is kept fixed in the simulation and the layer is moved upwards.

Model Geometry

The model background is described by $\sigma = 10^{-10}$ S/m and $\varepsilon_r = 4$ and the layer by $\sigma = 10^{-6}$ S/m and $\varepsilon_r = 7$, a setup typical for cold ice-dust mixtures with intervening water ice sheets. The chosen dielectric properties are consistent with those determined from laboratory experiments conducted at various temperatures and frequencies using mixtures of H_2O and CO_2 ice with soil (Pettinelli et al. 2003) and dry powders of dunite, montmorillonite, and kaolinite (Herique et al. 2002). Such granular dust particles are considered as best available analog material for the refractory component of comets in terms of composition and grain size distribution. Their formation on top of an initially homogeneous,

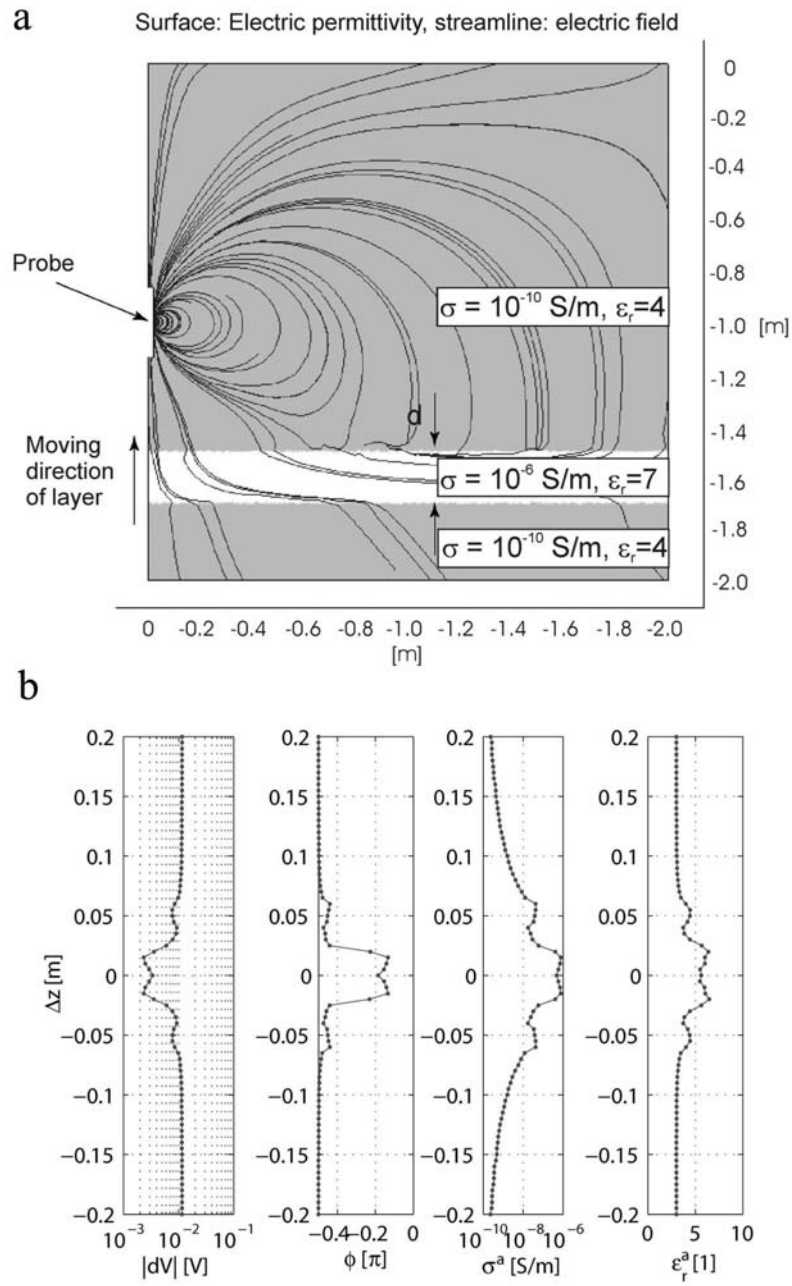

Fig. 6. a) Simulation of a vertical log through a buried horizontal layer of anomalous electric parameters. To simplify the simulation process, the layer is moved instead of the probe. b) Potential difference ΔV and phase ϕ measured at the receivers RX (left) and converted properties apparent conductivity σ^a and apparent relative permittivity ε_r^a (right) for different positions Δz of the layer with respect to the center of the probe.

sublimating ice-dust mixture was investigated in the frame of the KOSI comet simulation experiment, then performed in the Space Simulator at DLR Cologne, which considerably improved the general understanding of cometary activity (Gruen et al. 1993). Moreover, ice-dust mixtures of various ices, mostly H_2O and CO_2, were found to develop a layered structure beneath a dust cover. The near-surface layer of a cometary nucleus may evolve similarly, when heated during perihelion passage (Seiferlin et al. 1995). We therefore consider the case of an intervening water ice layer the initial thickness of which is arbitrarily chosen to be $d = 0.1$m thick.

Spatial Resolution

The two left-hand subplots of Fig. 6b show the potential difference ΔV and phase ϕ measured at the receivers RX. The signature of the anomalous water ice layer projected on the apparent quantities consists of a

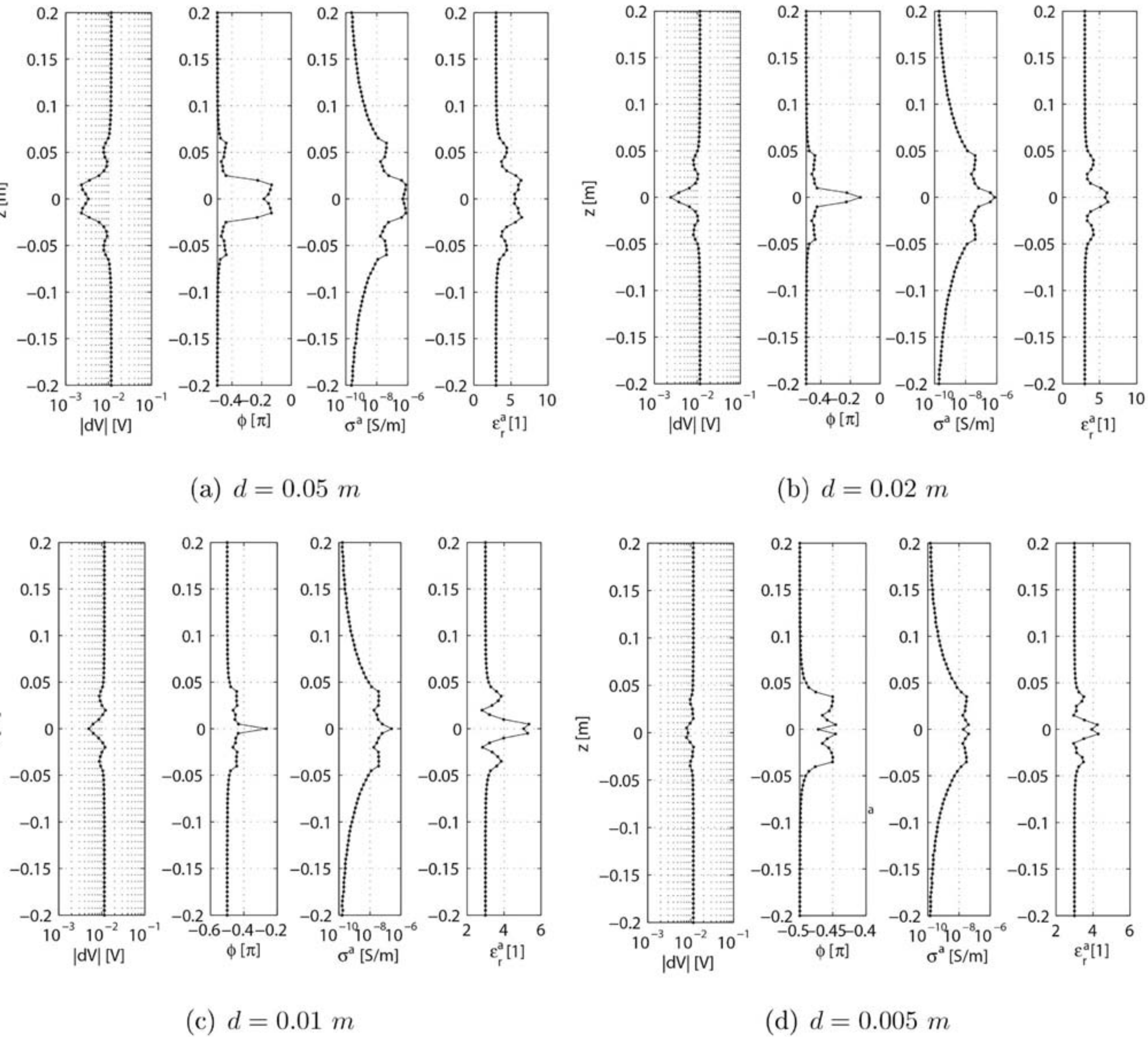

Fig. 7. Signal observed during penetration through a thin layer. The thickness of the layer d decreases from a) d = 0.05 m via b) d = 0.02 m and c) d = 0.01 m to d) d = 0.005 m. In subplot (a), the real material parameters are fairly well represented by the apparent electrical values. In subplots b) to d) this representation becomes increasingly inadequate. Note the complicated patterns at the parameter contrasts, i.e., the layer boundaries.

complicated pattern which is produced by the electrodes successively encountering the upper and lower electric contrast and superposing their individual responses according to their sensitivity distribution. The two right-hand subplots of Fig. 6b show ε_r^a and σ^a according to Equations 1 and 2. Since the layer's thickness is 0.1 m, the two transitions (background—layer and layer—background) are clearly distinguishable in the apparent quantities for the chosen electrode spacing of 0.01 m. In the central part, the true material parameter values of the anomalous layer of $\varepsilon_r = 7$ and $\sigma = 10^{-6}$ S/m are reasonably well recovered by the apparent quantities. Note, however, that the total length of the probe's electrode array sums up to 0.07 m (cf. right-hand subplot of Fig. 3) and that there is still a significant influence of the anomalous layer on the apparent quantities at a distance of three times the layer thickness $\Delta z \approx \pm$ 0.15 m.

This will be pointed out even more clearly by the following experiment where the layer thickness of the model introduced above is progressively decreased. Figure 7 displays four sets of data logs each in the manner of Fig. 6b. The layer thickness 5 is decreased stepwise from d = 0.05 m (a), d = 0.02 m (b), d = 0.01 m (c) to d = 0.005 m (d). The central part where the real material parameters $\varepsilon_r = 7$ and $\sigma = 10^{-6}$ S/m are well recovered by the apparent quantities shrinks and is barely visible for d = 0.02 m in Fig. 7b. The 0.01 m and 0.005 m thick

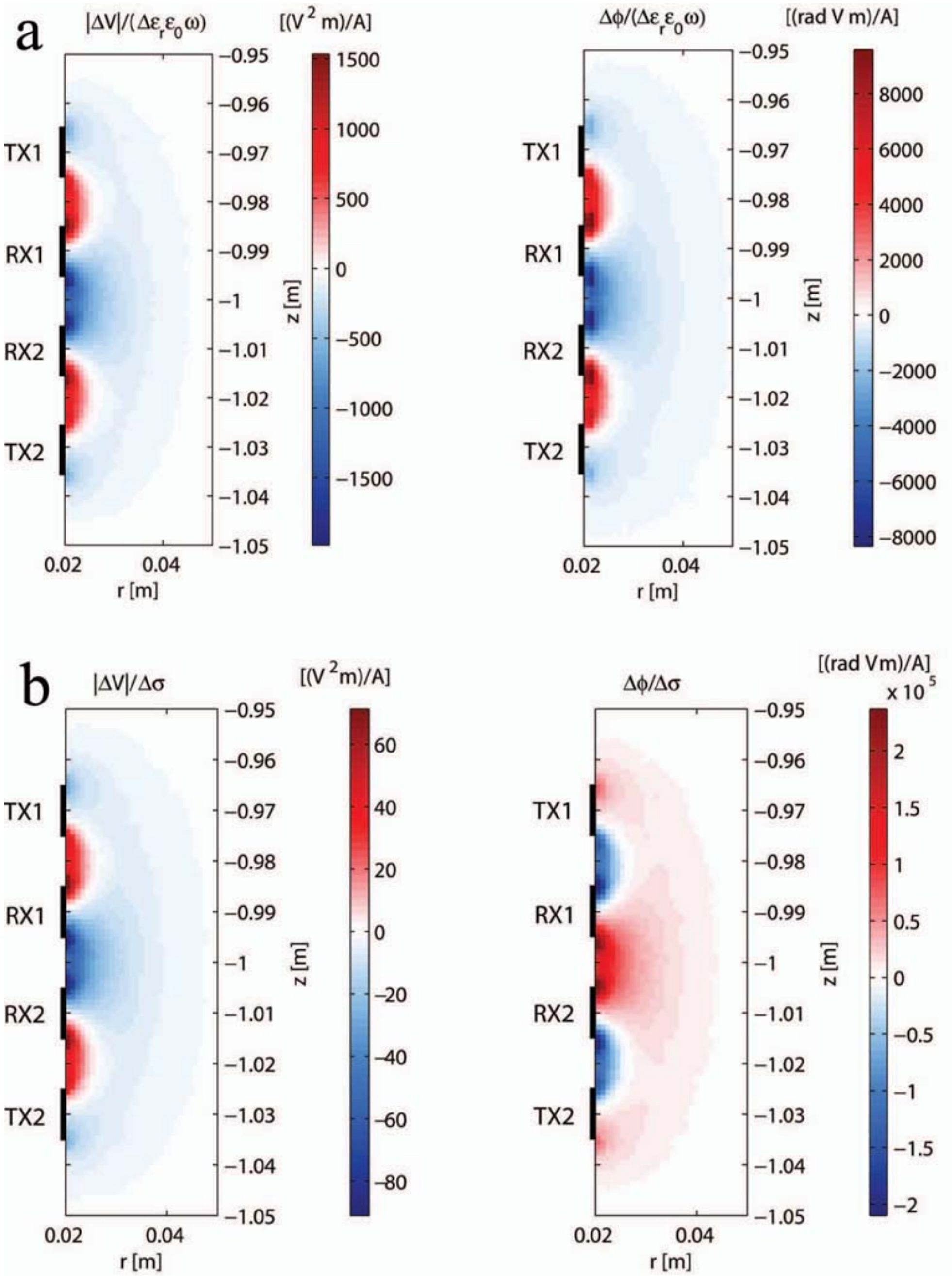

Fig. 8. Measurement sensitivities of the absolute values of potential difference $|\Delta V|$ (left) and phase ϕ (right) with respect to changes of (a) relative permittivity ε_r and (b) conductivity σ at a frequency of $f = 1$ kHz. Whereas the voltage measurement is rather affected by the dielectric constant, the phase measurement is more sensitive to the conductivity.

layers are not able to produce apparent permittivities and conductivities resembling the given material values. This simple virtual experiment leads to the following findings: 1) Apparent electrical properties are relevantly reflecting the material properties only within sufficiently homogeneous environments or within structures that exhibit spatial scales comparable with the electrode layout. Although this particular sequence of layer thicknesses is constrained to a narrow range it clearly shows the transition from meaningful apparent electrical values to rather insignificant ones. 2) The electrical response pattern is much more complicated than the true model (which is a simple horizontal layer) when sharp parameter contrasts are encountered. 3) There is need to perform three-dimensional simulations in future to take into account the effects of arbitrary structures. 4) The apparent quantities ε_r^α and σ^α are not sufficient to give a clear picture of the true model even in case of simple horizontal layers. Therefore, inversion methods are required for spatial reconstruction.

Measurement Sensitivity

The perturbation method has been employed to calculate the spatial distribution of measurement sensitivities. Each model parameter has been changed by 5%. The model background is $\sigma = 10^{-8}$ S/m and $\varepsilon_r = 4$. Figure 8 shows the spatial distribution of the sensitivities of the potential difference $|\Delta V|$ and the phase ϕ with respect to changes of the relative permittivity ε_r and the conductivity for a frequency of $f = 1$ kHz. The pattern resembles the *dc* sensitivity distribution (Spitzer 1998). The region dominating the response is comparable with the separation of the electrodes. Looking at the absolute values of the sensitivities it becomes obvious that the potential difference ΔV at the receivers RX is mainly influenced by the relative permittivity ε_r, whereas the phase ϕ is dominated by the electric conductivity σ.

CONCLUSIONS AND OUTLOOK

We have developed a 2D adaptive unstructured grid finite element forward modeling software to simulate the response of a permittivity probe. These measurements, if carried through in the uppermost few meters of asteroid and cometary soils, would not only place important constraints on environmental conditions close to the landing site, but could also be compared to regolith layers on other bodies in terms of stratigraphy, maturity, composition, and evolution. First, measuring depth profiles of complex permittivity may help establish the stratigraphy of near-surface regions of asteroids and comets. Second, the depth distribution of dielectric number and electrical conductivity then permits to deduce the porosity, composition, and subsurface moisture gradients. Third, the asymptotic permittivity values reached at low frequencies and the frequency range of the main transition region can be used to characterize the water ice content and the temperature of the shallow subsurface (Seidensticker et al. 2007). Finally, in situ measurements of the electrical properties of near-surface regions would impose important boundary conditions for inverting long-wavelength radio signals propagating through asteroid and cometary interiors for deep internal structure (Kofman et al. 2007).

The applicability of the mutual impedance technique to measure the complex permittivity of materials of planetological interest has been demonstrated by various laboratory studies and field tests in the past (e.g., Grard and Tabbagh 1991; Trautner and Grard 2003). The mutual impedance technique is preferable over conventional resistivity and capacitive permittivity measurements in planetary environments since 1) it is not required that the electrodes are in galvanic contact with the surrounding material; 2) there are no firm constraints on array configuration and electrode shape; 3) the electrical conductivity and dielectric number of the regolith can be determined simultaneously from measuring the complex permittivity. However, the measurement precision of the mutual impedance technique in the absence of dielectric loss is limited by the accuracy of phase measurements at low frequency (Trautner and Grard 2002). We were able to verify the chosen non-inductive approach in the frequency range 10^2 Hz $< f < 10^6$ Hz for electrical conductivities of $\sigma = 10^{-8}$ S/m.

Moreover, we may carry out a wide variety of virtual experiments taking into account inductive effects whenever they occur. This is especially helpful for studying the physical response in heterogeneous media. In perspective, we want to extend our simulations to 3D, evaluate the possibility of applying spatial reconstruction techniques for the electric material properties, and carry out resolution studies under the following constraints: 1) The available electric power for planetary field surveys is likely to be very low. 2) The payload is restricted to an absolute minimum. Hence, using numerical simulation the experimental design may carefully be examined and additional electrodes may be positioned well directedly, e.g., using the feet of the landers. This indeed results in surveys with sparse data sampling and limited spatial range. Still, rocks or ice lumps that are not penetrated directly might be resolved in the target area if the survey is carefully designed. Concluding, even coarse 3D models revealing structures embedded in the regolith will provide valuable information on the near-surface regions of asteroids and comets.

Acknowledgments–We are grateful to Essam Heggy who provided preprints of his work. An anonymous reviewer is thanked for valuable comments helping to substantially improve the manuscript.

Editorial Handling—Dr. Louise Prockter

REFERENCES

Benderitter Y., Jolivet A., Mounir A., and Tabbagh A. 1994. Application of the electrostatic quadrupole to sounding in the hectometric depth range. *Journal of Applied Physics* 31:1–6.

Benkhoff J. and Huebner W. F. 1995. Influence of the vapor flux on temperature, density, and abundance distributions in a multicomponent, porous, icy body. *Icarus* 114:348–354.

Carley R. A. and Heggy E. 2007. Finite difference time domain simulation of radar wave propagation through comet nuclei models. *Meteoritics & Planetary Science* 43. This issue.

Carrier W., Olhoeft G., and Mendell W. 1991. Physical properties of the lunar surface. In *Lunar source book: A user's guide to the Moon*, edited by Heiken G. H., Vaniman D. T., and French B. M. Cambridge: Cambridge University Press. pp. 475–567.

Chapman C. R. 2004. Space weathering of asteroid surfaces. *Annual Review of Earth and Planetary Science* 32:539–567.

Grard R. 1990. A quadrupolar array for measuring the complex permittivity of the ground: Application to earth prospection and planetary exploration. *Measurement Science and Technology* 1: 295–301.

Grard R. and Tabbagh A. 1991. A mobile four-electrode array and its application to the electrical survey of planetary grounds at shallow depths. *Journal of Geophysical Research* 96:4117–4123.

Gruen E., Gebhard J., Bar-Nun A., Benkhoff J., Dueren H., Eich G. 1993. Development of a dust mantle on the surface of an insolated ice-dust mixture—Results from the KOSI-9 experiment. *Journal of Geophysical Research* 98:15,091–15,104.

Hamelin M., Grard R., Laakso H., Ney R., Schmidt W., Simoes F. et al. 2004. Conductivity and dielectric characteristics of planetary surfaces measured with mutual impedance probes: From Huygens and Rosetta lander to Netlanders and future missions. In *Tools and technologies for future planetary exploration*, edited by Battrick B. pp. 169–174.

Heggy E., Asphaug E., Carley R., Safaeinili A., and Righter K. 2006. Dielectric properties of chondrites and their implication in radar sounding of asteroid interiors. LPI Contribution 1325. Houston, Texas: Lunar and Planetary Institute. pp. 45–46.

Herique A., Gilchrist J., Kofman W., and Klinger J. 2002. Dielectric properties of comet analog refractory materials. *Planetary and Space Science* 50:857–863.

Housen K. R. and Wilkening L. L. 1982. Regoliths on small bodies in the solar system. *Annual Review of Earth and Planetary Science* 10:355–376.

Kochan H., Hamacher H., Richter L., Hirschmann L., Assanelli S., Nadalini R., Pinna S., Gromov V. V., Matrossov S., Yudkin E. N., Coste P., Pillinger C., and Sims M. 2001. The Mobile Penetrometer (Mole)—A tool for planetary sub-surface investigations. In *Penetrometry in the solar system*, edited by Kömle N., I., Kargl G., Ball A. J., and Lorenz R. D. Graz, Austria: Space Research Institute, Austrian Academy of Sciences. pp. 212–243.

Kofman W., Barbin Y., Klinger J., Levasseur-Regourd A.-C., Barriot J.-P., Hérique A. et al. 1998. Comet nucleus sounding experiment by radiowave transmission. *Advances in Space Research* 21: 1589–1598.

Kofman W., Herique A., Goutail J.-P., Hagfors T., Williams I. P., Nielsen E. et al. 2007. The Comet Nucleus Sounding Experiment by Radiowave Transmission (CONSERT): A short description of the instrument and of the commissioning stages. *Space Science Reviews* 128:413–432.

Martinez A. and Byrnes A. P. 2001. Modeling dielectric-constant values of geologic materials: An aid to groundpenetrating radar data collection and interpretation. *Current Research in Earth Sciences* 247. Part 1.

Möhlmann D. 1994. Surface regolith and environment of comets. *Planetary and Space Science* 42:933–937.

Pettinelli E., Vannaroni G., Cereti A., Paolucci F., Della Monica G., Storini M. et al. 2003. Frequency and time domain permittivity measurements on solid CO_2 and solid CO_2-soil mixtures as Martian soil simulants. *Journal of Geophysical Research* 108:8029.

Richter L., Coste P., Gromov V. V., Kochan H., Nadalini R., Ng T. C., Pinna S., Richter H.-E., and Yung K. L. 2002. Development and testing of subsurface sampling devices for the Beagle 2 Lander. *Planetary and Space Science* 50:903–913.

Seidensticker K. J., Möhlmann D., Apathy I., Schmidt W., Thiel K., Arnold W., Fischer H.-H., Kretschmer M., Madlener D., Péter A., Trautner R., and Schieke S. 2007. Sesame—An experiment of the Rosetta lander Philae: Objectives and general design. *Space Science Reviews* 128:301–337.

Seiferlin K., Spohn T., and Benkhoff J. 1995. Cometary ice texture and the thermal evolution of comets. *Advances in Space Research* 15:35–38.

Spitzer K. 1998. The three-dimensional DC sensitivity for surface and subsurface sources. *Geophysical Journal International* 134: 736–746.

Spohn T., Seiferlin K., Hagermann A., Knollenberg J., Ball A. J., Banaszkiewicz M., Benkhoff J., Gadomski S., Gregorczyk W., Grygorczuk J., Hlond M., Kargl G., Kührt E., Kömle N., Krasowski J., Marczewski W., and Zarnecki J. C. 2007. Mupus—A thermal and mechanical properties probe for the Rosetta lander Philae. *Space Science Reviews* 128:339–362.

Telford W., Geldert L., and Sheriff R. 1995. *Applied geophysics.* Cambridge: Cambridge University Press. 348 p.

Trautner R. and Grard R. 2002. Measuring the electric properties of planetary environments with mutual impedance (MI) probes. In *Earth-like planets and moons*, edited by Foing B. H. and Battrick B. pp. 105–107.

Trautner R. and Grard R. 2003. Detection of surface ice and water deposits on Mars with a mutual impedance probe. *Journal of Geophysical Research* 108:8047, doi:10.1029/2002JE002008.

Trautner R., Simões F., Grard R., and Hamelin M. 2004. A new instrument for measuring the low-frequency electrical properties of planetary subsurface materials. In *Tools and technologies for future planetary exploration*, edited by Battrick B. pp. 193–196.

Veverka J., Farquhar B., Robinson M., Thomas P., Murchie S., Harch A. et al. 2001. The landing of the NEAR-Shoemaker spacecraft on asteroid 433 Eros. *Nature* 413:390–393.

Yano H., Kubota T., Miyamoto H., Okada T., Scheeres D., Takagi Y., Yoshida K., Abe M., Abe S., Barnouin-Jha O., Fujiwara A., Hasegawa S., Hashimoto T., Ishiguro M., Kato M., Kawaguchi J., Mukai T., Saito J., Sasaki S., and Yoshikawa M. 2006. Touchdown of the Hayabusa spacecraft at the Muses Sea on Itokawa. *Science* 312:1350–1353.

APPENDIX A

Using finite elements Equations 7 and 8 are represented by a system of integral equations according to the weak formulation

$$\int_\Omega \nabla\gamma \cdot (i\omega\tilde{\sigma}\vec{A} + \tilde{\sigma}\nabla V)\, d\Omega - \int_\Gamma \gamma \vec{j}_n \cdot d\vec{\Gamma} = 0 \quad \text{(A1)}$$

$$\int_\Omega \vec{\tau}[i\omega\tilde{\sigma}\vec{A} + \tilde{\sigma}\nabla V]d\Omega + \int_\Omega \nabla\times\vec{\tau}\cdot\left(\frac{1}{\mu}\nabla\times\vec{A}\right) \quad \text{(A2)}$$
$$d\Omega + \int_\Gamma \vec{\tau}\left[\vec{n}\times\left(\frac{1}{\mu}\nabla\times\vec{A}\right)\right]d\vec{\Gamma} = 0$$

which forms the basis for the subsequent discretization; γ and $\vec{\tau}$ ~ are arbitrary scalar or vector test functions, respectively. The integration is carried out over the domain Ω. To achieve uniqueness of the solution, a Coulomb gauge $\nabla\cdot\vec{A} = 0$ is applied. The solution for V and $\vec{A}$ are sought so that Equations A1 and A2 hold for all test functions γ and $\vec{\tau}$. The integrals over the boundary Γ of the domain Ω are defined using boundary conditions for the derivative of the electric potential in the normal direction $\vec{j}_n = \tilde{\sigma}\partial_n V + i\omega\tilde{\sigma}\vec{A}\cdot\vec{n}$ and the tangential component of the magnetic field $\vec{n}\times\vec{H} = \vec{n}\times\left(\frac{1}{\mu}\nabla\times\vec{A}\right)$ is the outward normal on the boundary. The finite element discretization of Equations A1 and A2 leads to a coupled system of linear equations

$$\begin{pmatrix} \mathbf{S} \\ \mathbf{R} \end{pmatrix} \cdot \begin{pmatrix} \vec{a} \\ \vec{\upsilon} \end{pmatrix} = 0 \tag{A3}$$

where **S** and **R** are the coefficient matrices corresponding to Equations A1 and A2, respectively. $\vec{a}$ and $\vec{\upsilon}$ are the solution vectors for the scalar potential at all nodes and the component of the magnetic vector potential along the edges of the elements, respectively. Using mixed boundary conditions for the electric potential and the magnetic vector potential at the outer boundaries we could significantly reduce the error propagating from the boundaries into the domain. The source currents are provided through inhomogeneous Neumann boundary conditions for the electric potential at the surface of the current electrodes TX. Equations A1 and A2 are discretized in two-dimensional cylindrical symmetry using the finite-element package COMSOL Multiphysics in combination with Matlab programming.